

Villification of the intestinal epithelium is driven by Foxl1 through activation of PDGFR α and BMPs

Received: 8 August 2024

Accepted: 6 February 2026

Published online: 24 February 2026

 Check for updatesGuoli Zhu^{1,2}, Galina Rozenberg^{1,2}, Deeksha Lahori^{1,3}, Jonathan Schug^{1,3}, Mark Tigue¹, Lan Cheng^{1,3,4}, Kirill Batmanov^{1,3} & Klaus H. Kaestner^{1,2,3} ✉

The primitive gut tube of mammals initially forms as a simple cylinder consisting of the endoderm-derived, pseudostratified epithelium and the mesoderm-derived surrounding mesenchyme. During mid-gestation, a dramatic transformation occurs in which the epithelium is both restructured into its final cuboidal form and simultaneously folded and refolded to create intestinal villi and intervillus regions. Here, we show that the mesenchymal winged helix transcription factor Foxl1, itself induced by epithelial hedgehog signaling, controls villification by activating BMP and PDGFR α and the planar cell polarity factor Fat4 in epithelial-adjacent telocyte progenitors either directly or indirectly. In the absence of Foxl1-dependent mesenchymal signaling, villus formation and the separation of epithelial cells into mitotic intervillus and postmitotic villus are delayed, and the differentiation of secretory progenitors temporarily blocked. Thus, Foxl1 orchestrates key events during the epithelial transition of the fetal mammalian gut.

The surface area of the human small intestine measures about 30 m², or the size of half a badminton court¹. This large area is required to enable effective digestion and absorption of nutrients. Villification, or the formation of intestinal villi that project into the gut lumen, is the major factor responsible for this increase in surface area (compared to a flat epithelium by close to 100-fold)¹. Remarkably, while villi are a feature of the small intestine in both mammals and birds, they arise by divergent morphogenetic mechanisms. Villus formation in birds is dependent on the sequential formation of first inner circular, then longitudinal, and finally muscularis mucosa muscles, which coincide with the appearance of epithelial ridges, zigzags, and villi, respectively^{2–4}. In contrast, mammalian villus formation can proceed in the absence of tensile forces generated by intestinal muscles; rather, it is dependent on PDGFR α (platelet-derived growth factor receptor alpha)/BMP (bone morphogenetic protein) positive mesenchymal cell clusters⁵, which themselves are induced by epithelial hedgehog signaling^{6,7}.

While initially epithelial progenitors are spread uniformly along the gut tube, as villi form, stem cells become restricted to intervillus regions driven by reciprocal signaling between the epithelium and underlying mesenchyme^{8,9}. Sonic hedgehog (Shh) signals become locally concentrated through epithelial folding, which has been proposed to involve intraepithelial compressive forces from rounding of mitotic cells⁸. Locally confined Shh signals induce the aforementioned BMP-expressing villus clusters in the mesenchyme². The critical role of BMP signaling in villus cluster formation was established by explant cultures of presumptive small intestine from 13.5 dpc (days post conception) embryos treated with localized sources of BMP or the pan-BMP inhibitor dorsomorphin¹⁰. More recently, it was demonstrated that the symmetry of the primitive gut tube is broken by mesenchymal tissue fluidization enabled by matrix metalloproteases, which initiate epithelial folding at the interface between PDGFR α ^{High} and PDGFR α ^{Low} mesenchyme¹¹. In this model, increased surface tension in the PDGFR α ^{High} tissue provides the

¹Department of Genetics, Perelman School of Medicine, University of Pennsylvania, Philadelphia, PA, USA. ²Digestive and Liver Center, Perelman School of Medicine, University of Pennsylvania, Philadelphia, PA, USA. ³Institute for Diabetes, Obesity, and Metabolism, Perelman School of Medicine, University of Pennsylvania, Philadelphia, PA, USA. ⁴Department of Cell and Developmental Biology, Perelman School of Medicine, University of Pennsylvania, Philadelphia, PA, USA. ✉e-mail: kaestner@penncmedicine.upenn.edu

driving force to establish mesenchymal villus clusters described previously^{5,7,12}.

At the onset of villification, also termed ‘epithelial transition’, the endoderm-derived epithelium forms a simple tube of pseudostratified cells with a layer thickness of ~50 μm. This pseudostratified epithelium, characterized by cell cycle-dependent interkinetic nuclear migration⁹, then changes to a columnar epithelium coincident with villus formation. Of note, adult *Lgr5*-positive intestinal stem/progenitor cells surprisingly have their origin in both nascent intervillus and villus regions, as the fetal epithelium undergoes massive remodeling and fission, which relocates epithelial cells from the non-proliferative pre-villus zone into the proliferative intervillus regions¹³.

As introduced above, the induction of villus formation and the formation of villus clusters in the underlying mesenchyme are dependent on epithelial to mesenchymal hedgehog signaling. Thus, both Sonic Hedgehog (Shh) and Indian Hedgehog (Ihh) are expressed in the epithelium, while the hedgehog receptors (Ptch1 and Ptch2) as well as the downstream transcription factor *Gli1* are expressed in the mesenchyme^{14,15}. Because the two epithelial hedgehog proteins are partially redundant, Madison and colleagues used the pan-hedgehog inhibitor Hhip to demonstrate that suppression of hedgehog signaling impaired villus formation, partially due to decreased BMP expression in the underlying mesenchyme¹⁴.

The winged helix transcription factor *Foxl1* (formerly termed *Fkh6*) is expressed in the first one to two cell layers of the mesenchyme juxtaposed to the epithelium before villus formation, originally shown by mRNA in situ hybridization¹⁵ and recently confirmed by immunofluorescence staining¹⁶. In addition, mice null for *Foxl1* exhibit delayed villus formation and a defect in the inhibition of epithelial proliferation in nascent villi, suggesting *Foxl1* is an important transcription factor controlling mesenchymal to epithelial signaling¹⁵. A link to epithelial hedgehog signaling was subsequently established via identification of functionally relevant binding sites for the hedgehog-dependent *Gli* transcription factors within an evolutionarily ultra-conserved enhancer at the *Foxl1* locus¹⁷. Furthermore, *Foxl1* expression was induced in fetal gut mesenchyme explants treated with Shh, while its mRNA levels were reduced in mice deficient for the hedgehog dependent transcription factors *Gli2* and *Gli3*¹⁷. Taken together, these findings suggest that *Foxl1* is a critical mediator of epithelial to mesenchymal crosstalk during villus formation. Here, we set out to determine the molecular targets and pathways controlled by *Foxl1* during intestinal villification.

Results

Our study comprised histological, ultrastructural, immunostaining, and molecular analyses during various stages of fetal intestinal development at the proximal, middle, and distal areas of the developing small intestine, as outlined in Fig. 1A. Note that overall intestinal length is reduced in the 15.5 dpc *Foxl1* null fetus (Fig. 1B), while the overall size of the fetus is not changed (data not shown). Immunostaining confirmed the absence of any *Foxl1* protein in the *Foxl1* null fetus, as expected (Fig. S1A). Histological analysis of the small intestine showed that while villus formation is progressing as expected in the anterior half of the small intestine in wild type fetuses at 15.5 dpc, this process is lagging in *Foxl1* deficient mice (Fig. 1C, D). The delay in villus formation is evident throughout the small intestine, though at 15.5 dpc it is most pronounced in the proximal and middle portions of the tissue, reflecting the anterior to posterior wave of villus formation (Fig. S1B). Even two days later, at 17.5 dpc, villification is abnormal in mutant mice (Fig. 1E, F), a phenotype that persists at 18.5 dpc (Figs. 1G, H; S2A). In order to investigate this phenotype in three dimensions, we performed scanning electron microscopy. As shown in Fig. 1I–N, in control mice, villification occurs through the formation of regularly spaced short invaginations into the gut lumen, which by 18.5 dpc have progressed to form elongated villi. This process is altered by loss of *Foxl1*, with absence of the regularly spaced nascent villi and the presence of

occasional long epithelial ridges at 15.5 dpc (yellow arrow in Fig. 1J), which persist until late gestation (Fig. 1L, N, red arrow; see also Fig. S3A). Abnormal epithelial ridges in the *Foxl1* null gut were further confirmed by immunostaining of small intestinal sections, which showed flat stretches of epithelial cells with the presence of *Olfm4*-positive cell clusters, which likely represent late induction of new proliferative intervillus regions (Fig. S3B). The presence of epithelial ridges instead of villi are reminiscent of the phenotype seen in small intestinal explants treated with the pan-BMP inhibitor dorsomorphin¹⁰, a connection we explore further below. By postnatal day 5, villus formation has mostly normalized in the mutant mice, with the occasional abnormally formed villus remaining (Figs. S2B, S4).

Fetal gut telocytes progenitors exist in two subpopulations

The inclusion of tdTomato in the recently developed *Foxl1* mutant allele employed here¹⁸ enabled us to follow the fate and determine the molecular properties of *Foxl1*-positive cells embryos heterozygous and homozygous for this *Foxl1* null allele. Of note, the *Foxl1* phenotype is recessive, as *Foxl1* heterozygous mice are indistinguishable from wild type controls^{15,19–21}. We performed scRNAseq on the proximal half of the small intestine of 15.5 dpc *Foxl1*^{CreER-tdTom/+} fetuses (Fig. 2A, B). As shown in the UMAP analysis in Fig. 2C and D, *Foxl1*⁺ cells segregate into two closely related cell clusters, which we termed ‘telocyte progenitors 1 and 2’. A list of marker genes for all cell populations shown in Fig. 2C is given in Supplementary Data 1. To investigate potential pseudo-temporal relationships between the telocyte progenitor 2 and progenitor 1 populations, we performed RNA velocity analysis²². This approach estimates the future transcriptional state of individual cells by leveraging the ratio of spliced to unspliced transcripts, thereby inferring likely trajectories of transcriptional change (see ‘Methods’ for details). This analysis suggests that telocyte 2 progenitors are precursors to both telocyte 1 progenitors as well as other, *Foxl1*-negative mesenchymal progenitor populations (Fig. 2E). Further support for this notion comes from analysis of the proliferation genes *Top2a*, *Birc5*, *Mki67* and *Pcna*, which are all expressed at higher levels in telocyte 2 progenitors (Fig. S5).

Telocyte progenitors 1 express high levels of *Pdgfra* and multiple *Bmp* mRNAs (Fig. 2F), and thus most likely correspond to ‘villus cluster cells’, i.e. the PDGFRα-positive cells important in villus formation originally identified by Karlsson and colleagues⁵. By exclusion, the telocyte progenitor 2 population likely represents *Foxl1*⁺ cells directly adjacent to the intervillus epithelium. Interestingly, we identified *Glp2r*, encoding the GLP-2 receptor, as another gene predominantly expressed in telocyte progenitor 1 cells, and confirmed the localization of the *Glp2r* mRNA to villus cluster cells by RNAscope analysis (Fig. 2G–I). An additional telocyte progenitor 1 marker is the Zinc-finger transcription factor Spalt like transcription factor 1 (*Sall1*), which is part of the NuRD transcriptional repressor complex (Fig. 2J–L). *Sall1*/*Foxl1* double positive cells can be seen to also mark a cluster of cells that appears to be in the process of initiating a new villus (Fig. 2L). Importantly, this single cell analysis clearly shows that *Foxl1*⁺ cells are distinct from myofibroblasts, interstitial cells of Cajal, and pericytes, identified by the expression of *Acta2*^{med}/*Myh11*^{med}/*Des*^{med}/*Tagln*^{med}, *Etv1*⁺/*Kit*⁺/*Acta*^{low}, and *Cspg4*⁺/*Pdgfrb*⁺/*Abcc9*⁺ or *Abcc9*⁺/*Ndufa4l2*⁺, respectively (Fig. 2C). Key marker genes used to identify the various cell clusters are highlighted in Figs. S6 and S7. Major hallmarks of the telocyte progenitor 1 and 2 populations are summarized in the graphic shown in Fig. 2M.

Expression of PDGFRα in telocyte progenitors is dependent on Foxl1

Next, we analyzed the expression profile of the fetal small intestine of *Foxl1* null (*Foxl1*^{CreER-tdTom/CreER-tdTom}) mice and compared them to those of heterozygous fetuses. The number of cells in each cluster by genotype is given in Supplementary Data 2, and the complete list of differentially

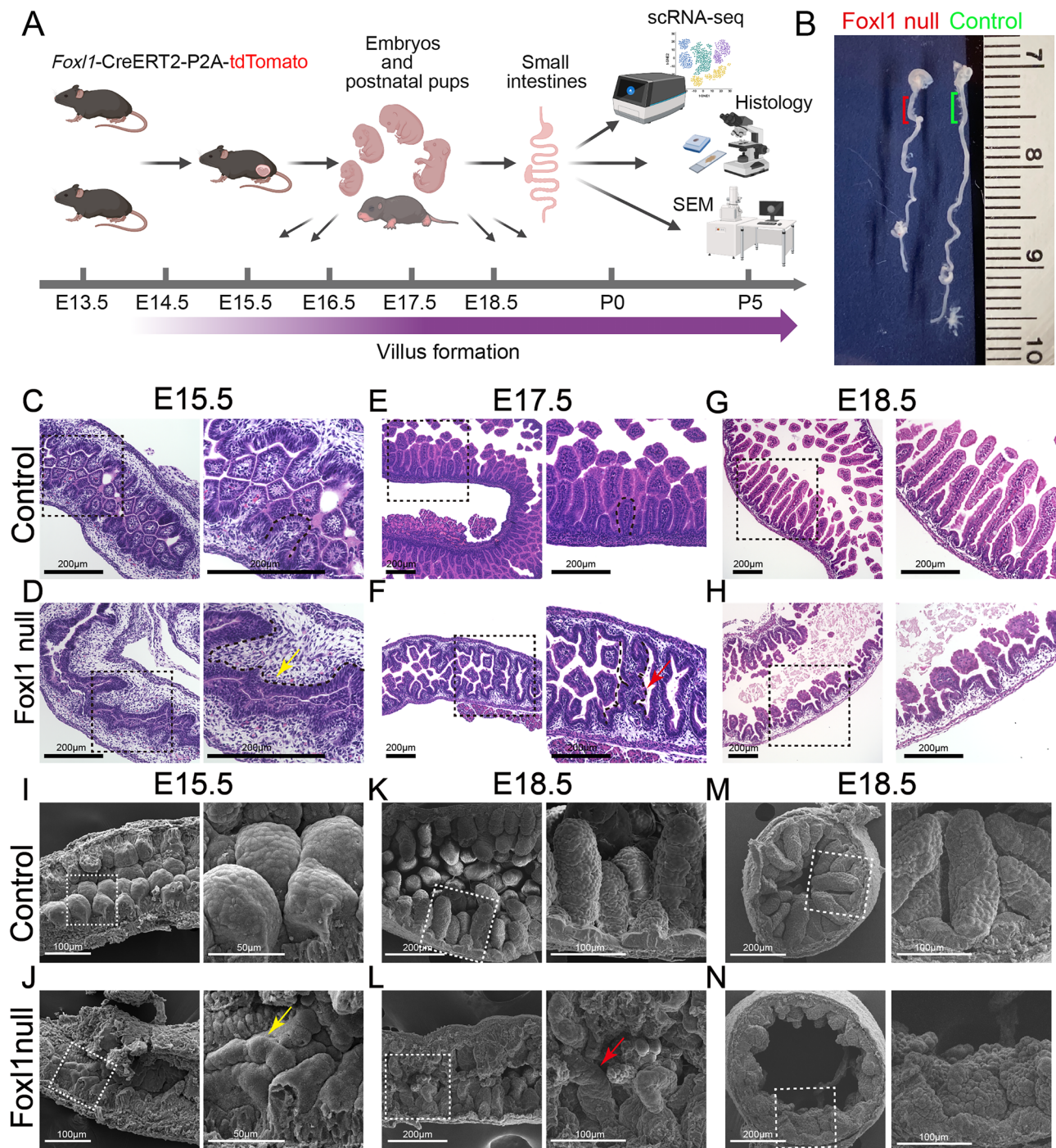
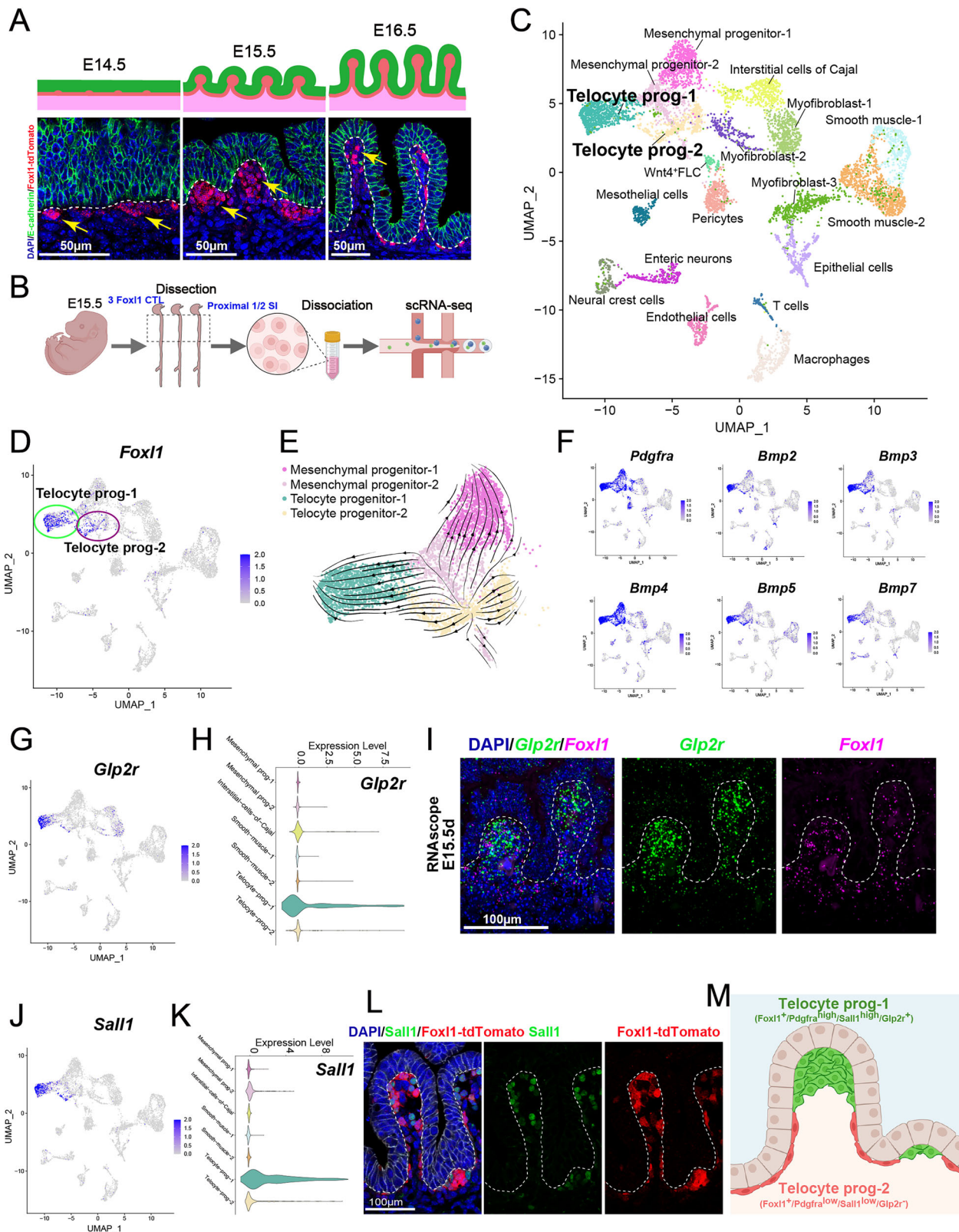


Fig. 1 | Intestinal villification is dependent on the winged helix transcription factor *Foxl1*. **A** Overview of experimental design. **B** Anatomy of the gastrointestinal tract of control and *Foxl1* null fetuses at 15.5 dpc. **C–H** Hematoxylin and eosin-stained small intestine from control (**C, E, G**) or *Foxl1* null (**D, F, H**) fetuses at the developmental stages indicated. The yellow arrow in **D** indicates lack of invagination, and the red arrow in **F** marks persistent epithelial ridges. **I–N** Scanning electron micrographs of small intestine from control (**I, K, M**) or *Foxl1* null (**J, L, N**)

fetuses at the developmental stages indicated. In all panels, larger magnification images shown on the right correspond to the areas outlined on the left. Magnification is indicated by scale bars. For histological and scanning electron microscopy analyses, 3–5 embryos per genotype at each developmental stage were examined, and representative images are shown. Panel A Created in BioRender. Kaestner, K. (2026) <https://BioRender.com/20knsx9>.

expressed genes is contained in Supplementary Data 3. Note that in the *Foxl1* null fetuses, the *cis*-regulatory elements CreER-tdTomato expression are still active, enabling us to visualize *Foxl1* telocyte progenitors, which are still localized to the mesodermal cell layer that is directly juxtaposed to the developing epithelium. Loss of *Foxl1* does not significantly affect telocyte progenitor number (Fig. 3A). The UMAP plots shown in Figs. 3B and S8 clearly demonstrate that the

telocyte progenitor 1 population is shifted in the *Foxl1* null intestine reflecting its altered expression profile; however, all cell types are present in all fetuses analyzed (Figure S8). Two of the telocyte progenitor 1 marker genes mentioned above, *Glp2r* and *Sall1*, are *Foxl1*-dependent, either directly or indirectly (Fig. S9A–D). As mentioned above, among the markers of the telocyte progenitor 1 cells is PDGFR α . The scRNAseq data shown in Fig. 3C, D as well as the



immunofluorescence staining presented in Fig. 3E demonstrate that PDGFR α expression is reduced in *Foxl1*-deficient telocyte 1 progenitors. Further support for a critical role for *Foxl1* as either direct or indirect upstream regulator of *Pdgfra* comes from whole-mount immunofluorescence staining (Fig. 3F), which shows the localization of PDGFR α ^{high} cells to villus cluster cells and their absence in *Foxl1* null fetuses. The full three-dimensional view of PDGFR α expression is

visualized by the supplementary videos 1 and 2. To determine if *Pdgfra* is a direct target of *Foxl1*, we performed Cut-and-Run assays on telocytes from 15.5 dpc fetal gut. However, we found no *Foxl1* binding event within 10 kb of the *Pdgfra* promoter (data not shown), suggesting that regulation might be indirect. Because villus formation is delayed but not completely blocked in *Foxl1* null mice, we hypothesized that PDGFR α ^{high} villus clusters might reappear at later stages of

Fig. 2 | Fetal FOXL1-positive telocyte progenitors partition into villus cluster and intervillus populations. **A** Foxl1-positive cells labeled by tdTomato expression reorganize during the epithelial transition, when the pseudostratified epithelium (E14.5) is converted to a simple cuboidal epithelium (E16.5). Epithelial cells are labeled with E-cadherin in green, Foxl1-positive cells by tdTomato in red. **B** Experimental outline for single cell RNAseq study. The proximal half of the E15.5 small intestine was used for the analysis. **C** UMAP plot of scRNAseq data identifies more than a dozen cell types. Foxl1-positive cells are labeled as telocyte progenitor 1 and 2. **D** UMAP plot showing that Foxl1 transcripts are confined to the telocyte progenitor clusters. **E** RNA velocity analysis suggests that telocyte progenitor 2 cells (yellow) give rise to both telocyte progenitor 1 cells as well as two Foxl1 negative mesenchymal cell populations. **F** UMAP plot of mRNA expression *Pdgfra* and several BMP genes in the two telocyte progenitor populations. **G** UMAP plot of mRNA abundance for *Glp2r*, encoding the receptor for the intestinotrophic hormone GLP-2. **H** Violin plot showing the enrichment of *Glp2r* transcripts in the telocyte progenitor 1 population. **I** RNAseq analysis of fetal mouse intestine from

E15.5 fetuses localizes *Glp2r* transcripts (green) and *Foxl1* mRNA (purple). **J** UMAP plot of mRNA abundance for *Sall1*, encoding the spalt like transcription factor 1, a zinc finger transcriptional repressor. **K** Violin plot showing the enrichment of *Sall1* transcripts in the telocyte progenitor 1 population. **L** Immunofluorescence staining of anterior small intestine from E15.5 fetuses with antibodies specific to *Sall1* (green) and Foxl1 (red) show localized expression in villus tip telocytes, as well as in a newly forming villus cluster. DAPI (blue) was used to visualize nuclei. **M** Model of relative positioning and prominent marker genes of telocyte progenitors 1 and 2 during intestinal villification. For imaging analyses (**A**, **I**, and **L**), 3–5 embryos per genotype at the indicated developmental stage were examined, and representative images are shown. Single-cell RNA sequencing was performed using small intestines from three embryos per genotype (E15.5), all collected from the same litter to ensure matched developmental stages and to minimize batch variability. Panel B Created in BioRender. Kaestner, K. (2026) <https://BioRender.com/wnlyvi4> Created in BioRender. Kaestner, K. (2026) <https://BioRender.com/utcw1bv>.

gestation. This is indeed the case, as shown by immunofluorescence staining of E18.5 embryos for PDGFR α (Fig. S10), suggesting the possibility that other transcription factors can activate the *Pdgfra* gene at later stages of development.

Foxl1 is required for activation of multiple Bmp genes in telocyte progenitor cells

Next, we focused on BMP proteins, as BMP signaling from the mesoderm to the epithelium is critical for villus cluster formation¹⁰. Telocyte-produced BMPs enriched in villus cluster cells signal to the adjacent endoderm to inhibit WNT signaling and limit proliferation (Fig. 4A). High expression of several BMP genes was present particularly in villus cluster telocyte-progenitor 1 cells (Fig. 4B). In the case of BMP4, expression also extends to Foxl1-negative mesenchymal progenitor cells; however, its levels are clearly reduced specifically in Foxl1-deficient telocytes (Fig. 4B). Transcript levels of *Bmp2*, *Bmp3*, *Bmp4*, *Bmp5* and *Bmp6* were all significantly reduced in the Foxl1 null telocyte progenitor 1 population (Fig. 4B). To determine if BMP signaling to the epithelium is impaired by this reduction in telocyte BMP expression, we performed immunostaining for phosphorylated SMAD1/5 (Fig. 4C). Nuclear pSMAD1/5 is clearly detectable in epithelial cells in the villus tip, but not intervillus regions in control embryos. In contrast, most epithelial cells in Foxl1 null mice are devoid of signal, confirming a reduction of active BMP signaling to the epithelium. When analyzing the pSMAD1/5 staining, we also noted signal in nuclei of mesenchymal cells within the invaginating villi, with most of them negative for Foxl1-tdTomato. These findings are expected given the previous report demonstrating that BMP-driven villus cluster formation occurs even in the absence of epithelial BMP receptors and thus has to rely on BMP signaling within the mesenchymal compartment¹⁰.

Loss of mesenchymal BMP signals is expected to result in de-inhibition of WNT signaling in the epithelium overlying villus cluster telocytes²³. Indeed, we found expression of the WNT target gene *Sox9* expanded from the developing intervillus regions to nascent villi in the Foxl1 null fetal intestine (Fig. 4D). Likewise, epithelial proliferation was not confined to the nascent intervillus regions but extended to the villus epithelium in mutant mice (Fig. 4D). This likely reflects the developmental delay in these mice, as prior to villus demarcation, all epithelial cells are proliferative. Of note, at later stages of development, both the Sox9-positive epithelial domain as well as the proliferative zone normalize in Foxl1 null mice, consistent with the overall normalization of the histological phenotype documented above (Fig. S11).

Foxl1 contributes to regulation of planar cell polarity genes

Patterning of the developing gut epithelium is temporarily perturbed in the absence of Foxl1, and the hyperproliferation of the epithelium due to lack of BMP signaling documented above regionally causes

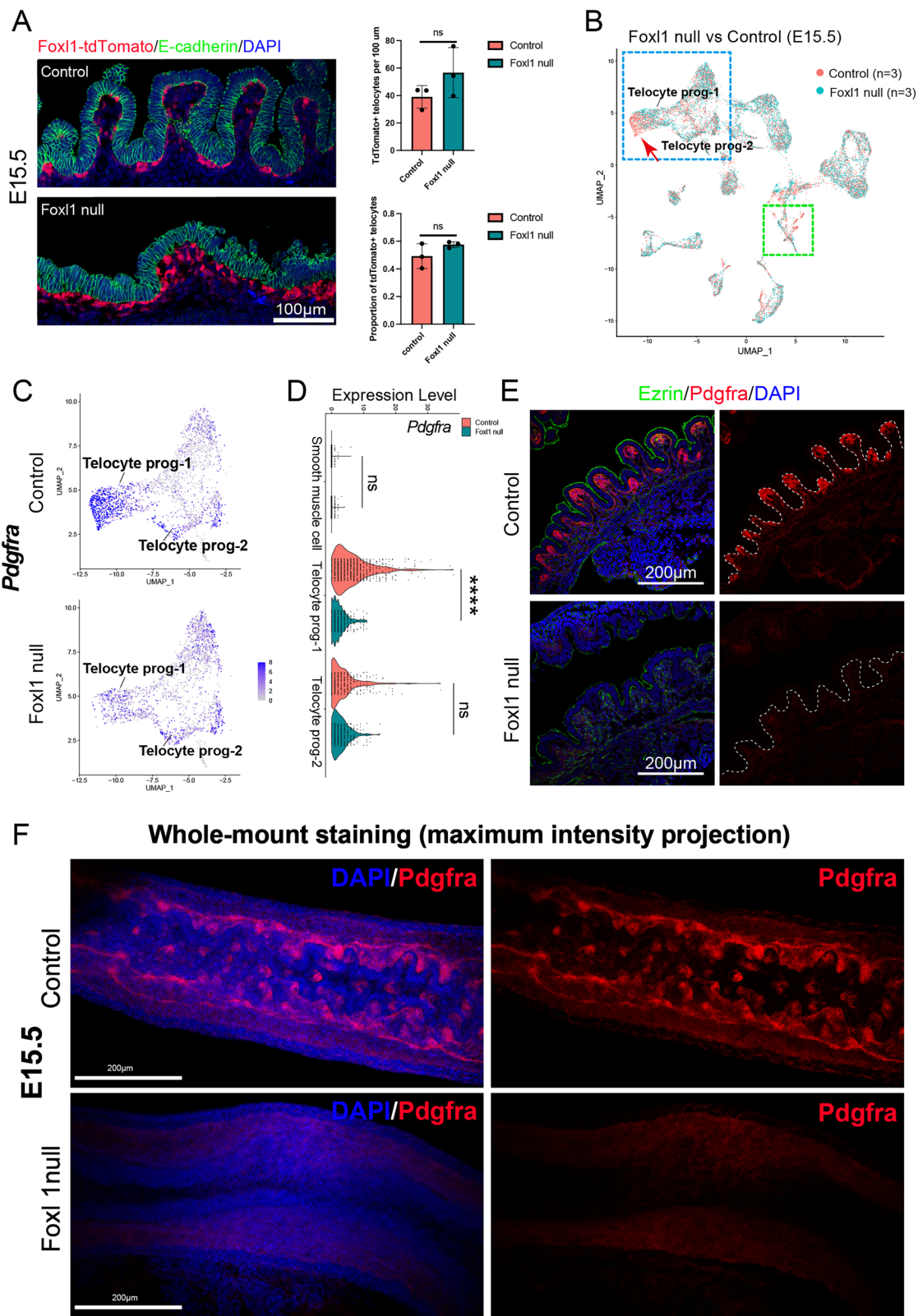
epithelial cells to be more than 100 μ m distal to the underlying stroma (Figs. 5A, S12A). A subset of the luminal-most epithelial cells undergoes apoptosis as indicated by cleaved caspase 3 staining (Fig. 5A) as well as the TUNEL assay (Fig. S12B). It was shown previously that after mitosis of epithelial cells, one daughter cell inherits the connection to the basement membrane from the mother cell, while the other daughter cell has to develop a new basal filopodium, a process that is dependent on *Wnt5a*²⁴. When this does not occur, the ‘connection-less’ epithelial cells undergo apoptosis.

Recently, planar cell polarity (PCP) genes were identified among mesenchymal Gli targets in the fetal gut, and it was further demonstrated that the GLI2 target gene *Fat4* is required for villus development during the epithelial transition²⁵. Rao-Bhatia and colleagues had found that the villification defects in mice with mutations in the PCP gene *Fat4* were preceded by a reduction in the number of epithelial T-folds, characteristic invaginations of the epithelium that form the boundaries of developing villi and that can be visualized by staining with the apical membrane marker Ezrin²⁵. In order to evaluate if loss of Foxl1 delays epithelial remodeling, we stained small intestinal sections from fetuses at developmental stages spanning villification (13.5 to 15.5 dpc; Fig. S12C) for Ezrin to identify T-folds and PDGFR α to label villus cluster cells. As shown in Fig. 5C, the number of T-folds is reduced in the Foxl1-deficient intestine of 14.5 dpc embryos, coinciding with the loss of PDGFR α expression in telocyte progenitors. Next, we employed staining for F-actin to assess the orientation of stromal cells in the developing intestine. As shown in Fig. 5D, while mesenchymal cells in the control fetal gut reorient their major axis to be parallel to the invaginating villi, this process fails to occur in Foxl1 null mice, supporting the notion of impaired planar cell polarity in stromal cells.

When analyzing expression of PCP genes using our scRNAseq data, we found that expression of *Fat4* was significantly reduced in Foxl1 null telocyte progenitor 1 cells, while that of the PCP genes *Vangl1* and 2 was not affected (Fig. 5E). We also found *Fat4* mRNA to be more abundant in smooth muscle cells; the significance of this observation is unknown (Fig. 5E). Using our Cut and Run data, we found Foxl1 binding in the promoter of *Fat4*, suggesting a direct regulatory relationship (Fig. 5F).

Loss of Foxl1 impacts epithelial gene expression profiles

As shown above, Foxl1 deficiency transiently impacts the patterning of the overlying epithelium, with many presumptive villus tip epithelial cells remaining in the cell cycle (Fig. 4D). We had also noted a shift in the UMAP pattern of epithelial cells between control and Foxl1 null cells in 15.5 dpc embryos (green box in Fig. 3B). To address this issue further, we re-clustered the epithelial cells from control mice only via UMAP. Fig. 6A shows that fetal gut epithelial cells of control embryos partition into two major groups, which we identified as ‘secretory progenitors’ and ‘undifferentiated epithelial cells’ based on their



expression profiles. The heatmap in Fig. 6B shows the 225 most differentially expressed genes between these two clusters (false discovery rate <10%; absolute fold-change >2), while Fig. 6C indicates selected marker genes for each cell type. Fetal secretory progenitors are characterized by high mRNA levels for transcription factors *Klf4*, *Spdef*, and *Sox4*, known to be critical for secretory cell differentiation^{26–28}. Undifferentiated epithelial cells, in contrast, exhibit

strong expression of *Sox9* (which marks them as proliferating inter-villus cells as seen in Fig. 4D) as well as markers of the absorptive enterocyte lineage (*Alpi*, the gene for intestinal alkaline phosphatase, *Fabp1*, encoding fatty acid binding protein 1, *Apoa4*, encoding Apolipoprotein A4 which is important in intestinal cholesterol absorption, and *Slc16a1*, encoding the monocarboxylic acid transporter for lactate).

Fig. 3 | Villus cluster PDGFR α expression is *Foxl1* dependent. **A** Telocytes labeled by tdTomato expression driven by the *Foxl1 cis*-regulatory elements (red) are retained in *Foxl1* null mice. Epithelial cells are labeled by E-cadherin (green). Quantification of the density of tdTomato-positive cells in mice heterozygous (control) or homozygous (*Foxl1*) for the *Foxl1*-tdTomato allele as either number of telocytes per linear distance or as proportion of submucosal cells. $N = 3$ embryonic day 15.5 embryos per genotype. Data are presented as mean \pm standard deviation. Statistical significance was assessed using an unpaired two-tailed t-test with Welch's correction. ns, $p = 0.2305$ (upper panel); ns, $p = 0.2452$ (lower panel). **B** UMAP plot of scRNAseq data comparing control and *Foxl1* null fetal gut shows dramatic shifts in both telocyte progenitor (blue box) as well as in epithelial cells (green box). Single cells are color-coded by genotype. Three embryos per genotype, all from the

same litter, were used. **C** UMAP plot showing *Pdgfra* expression in control and *Foxl1* null telocyte progenitors. **D** Violin plot of *Pdgfra* expression in control and *Foxl1* null telocyte progenitors. Cells identified as smooth muscle cells are shown for comparison. Statistical significance was assessed using a two-sided Wilcoxon rank-sum test. Smooth muscle cell: ns, $p = 0.77$; Telocyte prog-1: ****, $p < 2 \times 10^{-16}$; Telocyte prog-2: ns, $p = 0.71$. **E** Immunofluorescence labeling confirms dramatic reduction in PDGFR α expression (red) in the absence of *Foxl1*. The apical membrane of epithelial cells is stained for Ezrin (green). **F** Maximum intensity projection of anterior small intestine stained in whole mount with an antibody to *Pdgfra* (red), and counterstained with DAPI (blue) to label nuclei. For imaging analyses (**E**, **F**), 3–5 embryos per genotype at the indicated developmental stages were examined, and representative images are shown.

Next, we added epithelial cells from *Foxl1* null embryos to the UMAP plot and found that they are largely confined to the undifferentiated epithelial cell cluster (Fig. 6D). When we quantified the proportion of cells in each cluster, we found a striking loss of secretory progenitor cells in *Foxl1* null embryos (Fig. 6E). Finally, we performed gene set enrichment analysis to search for pathways that are differentially regulated in epithelial cells in the absence of telocyte *Foxl1*. As shown in Fig. 6F, the response to BMP signaling, negative regulation of epithelial proliferation, and establishment of planar cell polarity were all strongly enriched among the genes more highly expressed in the control gut epithelium, confirming that loss of telocyte *Foxl1* has a major, if transient, impact on the development of the fetal intestinal epithelium at this time-point. Finally, we confirmed these findings by immunofluorescent staining for markers of the secretory cell lineage. Antibody staining to detect AGR2 (Anterior gradient protein 2 homolog), a protein disulfide isomerase required for the formation of mixed disulfides in intestinal mucins (Fig. 6G, I), and its substrate MUC2 (Mucin2), the major mucin of intestinal goblet cells (Fig. 6H, J), demonstrated that both are expressed in the embryonic day 15.5 control intestine in secretory cell progenitors. However, the proportion of AGR2+ and MUC2+ cells is significantly reduced in the *Foxl1* null gut, confirming the findings from our single cell RNAseq analysis. The fact that the percentage of secretory cells labeled by MUC2 and AGR2 immunofluorescence staining is smaller than the percentage of secretory progenitors identified by RNAseq (compare Fig. 6H, J–E) is likely because the protein markers only detect the most mature secretory lineage cells, while RNAseq, using hundreds of transcript measurements, can assign lineage even to very immature secretory progenitors. Of note, this defect in secretory lineage specification in the *Foxl1* null gut is only transitory, as by embryonic day 18.5 the frequency of AGR2 and MUC2 positive cells has normalized (Fig. S13).

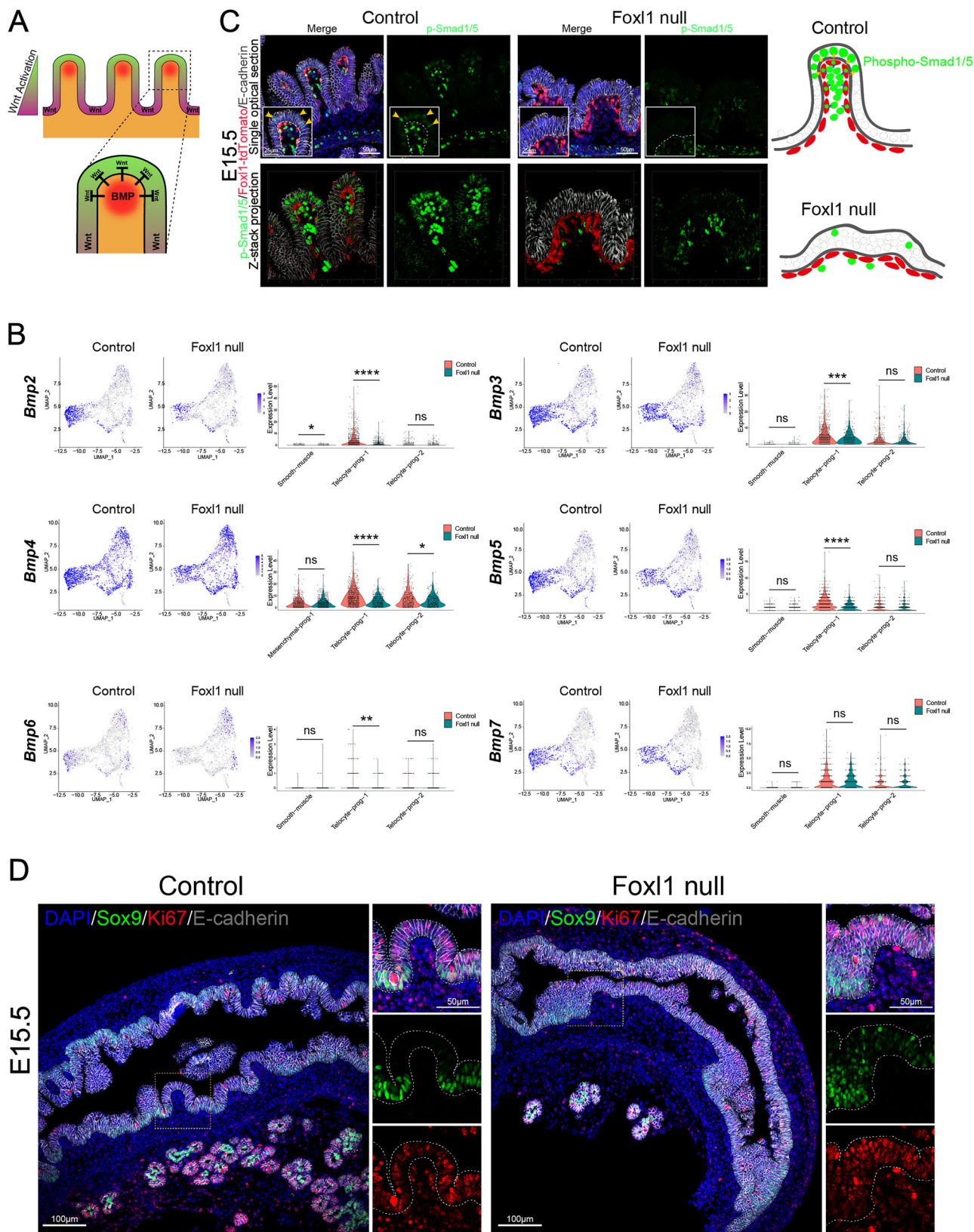
Discussion

Villus formation is an essential and fascinating process in vertebrate gut development and depends on reciprocal epithelial-to-mesenchymal crosstalk. Epithelial hedgehog proteins are among the earliest signals emanating from the endoderm during organogenesis of the gut. Consequently, inhibition of hedgehog signaling with neutralizing antibodies or ablation of either *Shh* (sonic hedgehog) or *Ihh* (Indian hedgehog) causes impairment of gut development and villus formation^{29,30}. Hedgehog proteins signal via their receptor Ptch1 (patched 1), expressed exclusively in the gut mesoderm, to stabilize the DNA-binding transcription factors Gli2 and Gli3. In 2006, computational analysis of evolutionarily conserved enhancers led to the identification of an ultra-conserved putative enhancer located between the neighboring *Foxl1* and *Foxf1* genes³¹. Previously, we identified seven Gli binding sites in this genomic region, some conserved from *Fugu* to human, and showed through in vitro and in vivo studies that both *Foxl1* and *Foxf1* are Gli target genes¹⁷. Here, we demonstrate that *Foxl1*-expressing telocyte progenitors are partitioned into two major subpopulations with distinct

gene expression profiles: telocyte progenitors 1 and 2 correspond to telocytes in villus clusters and those adjacent to developing intervillus regions, respectively. Cells we describe as “Telocyte progenitor 1” population have also been reported as PDGFR α ^{high} cells, and as shown above, PDGFR α expression is severely reduced in the absence of *Foxl1* (See Fig. 3C–F), indicative of a delay in the formation of villus clusters. Maimets and colleagues recently reported that PDGFR α ^{high} cells express genes that promote a WNT signaling gradient. Inhibition of WNT signaling during fetal life using a Porcupine inhibitor led to a massive reduction in villus formation³², as expected from the absolute requirement of telocyte Wnt for adult intestinal stem cell function³³.

Villification is significantly delayed in the absence of *Foxl1*, and abnormal proliferation persists in epithelial cells in the presumptive developing villi at 15.5 dpc, a developmental time-point when the anterior small intestine is already separating into intervillus regions and nascent villi. We attribute this to the loss of BMP signaling as multiple *Bmp* genes exhibit reduced expression in the absence of *Foxl1* and a delay in villus cluster formation. BMP signaling had been established by Walton and colleagues as key factor of villus formation^{7,10}. Of note, the defect is only temporary, and other transcription factors, currently unknown, compensate for *Foxl1* loss. One attractive candidate is the closely linked *Foxf1* gene, which like *Foxl1* is induced by hedgehog signaling from the epithelium¹⁷. Interestingly, heterozygous loss of *Foxf1* causes defects in mesenchymal to epithelial signaling reminiscent of the phenotype of *Foxl1* null mice³⁴. Because of the close linkage (~50 kb) of the two genes, a mouse null for both cannot be generated through intercrossing, and the analysis of *Foxl1/Foxf1* deficient telocytes will require the derivation of new conditional mouse models. Of note, loss of the telocyte transcription factor *Foxl1* has a transient secondary impact on the overlying epithelium, with a delay in secretory progenitor cell differentiation and temporary retention of proliferating epithelial cells overlying villus cluster cells.

Recently, planar cell polarity genes were identified among the mesenchymal Gli2 targets in the fetal gut, and it was demonstrated that the Gli2 target *Fat4* is required for villus development during the epithelial transition²⁵. The model of villification proposed by Rao-Bhatia and colleagues states that activation of Gli2 in telocyte progenitors opposite to the hedgehog-secreting epithelium is sufficient to activate *Fat4* and other planar cell polarity genes directly²⁵. Our data indicate that induction of *Fat4* in telocyte progenitors depends not only on Gli proteins but also on winged helix transcription factors. We document by scRNAseq analysis of the proximal small intestine of 15.5 dpc fetuses that expression of planar cell polarity genes including *Fat4* is enriched in *Foxl1*+ telocyte progenitor 1 cells and reduced significantly in the absence of *Foxl1* (Fig. 5E). Therefore, we propose a coherent feed-forward loop for the regulation of stromal planar cell polarity genes, in which Gli2 activates both *Foxl1* and *Fat4* (and related targets), while *Foxl1* also activates *Fat4* expression in epithelium-adjacent stromal cells.



In conclusion, we have shown that the deletion of the winged helix transcription factor Foxl1, expressed in endoderm-adjacent mesodermal telocyte progenitors, transiently delays the epithelial transition and ordered villus formation via the regulation of BMP, PDGFR α , and PCP signaling molecules.

Materials and methods

Mice

All animal procedures were approved by Institutional Animal Care and Use Committee of the Office of Animal Welfare at the University of Pennsylvania and conducted under protocol 804436. The mice used in

Fig. 4 | Loss of BMP expression and abnormal epithelial proliferation in the Foxl1-deficient fetal small intestine. **A** Model for partitioning of small intestinal epithelial cells into postmitotic villus cells and proliferating intervillus cells through BMP signals emanating from villus cluster cells. Modified after Shyer and colleagues². **B** Expression of multiple *Bmp* genes is reduced in telocyte progenitor 1 cells in the absence of Foxl1. UMAP and violin plots for telocyte progenitors 1 and 2 as well as smooth muscle cells or Mesenchymal progenitor-1 for comparison. Statistical significance was assessed using a two-sided Wilcoxon rank-sum test. Smooth muscle cells (Control vs Foxl1 null): *Bmp2*, *, $p = 0.047$; *Bmp3*, ns, $p = 0.140$; *Bmp4*, ns, $p = 0.382$; *Bmp5*, ns, $p = 0.66$; *Bmp6*, ns, $p = 0.147$. Telocyte prog-1 (Control vs Foxl1 null): *Bmp2*, ****, $p < 2 \times 10^{-16}$; *Bmp3*, ***, $p = 9.2 \times 10^{-4}$; *Bmp4*, ****, $p < 2 \times 10^{-16}$; *Bmp5*, ****, $p < 2 \times 10^{-16}$; *Bmp6*, **, $p = 0.0017$; *Bmp7*, ns, $p = 0.65$. Telocyte prog-2 (Control vs Foxl1 null): *Bmp2*, ns, $p = 0.312$; *Bmp3*, ns,

$p = 0.886$; *Bmp4*, *, $p = 0.024$; *Bmp5*, ns, $p = 0.52$; *Bmp6*, ns, $p = 0.703$; *Bmp7*, ns, $p = 0.17$. *, $p < 0.05$; **, $p < 0.01$; ***, $p < 0.001$; ****, $p < 0.0001$. **C** Determination of BMP signaling pathway activation by immunofluorescence staining for phosphorylated Smad1/5 (p-Smad1/5), downstream mediators of BMP receptor activation, in the fetal gut (E15.5). Shown are both single optical sections as well as z-stack projections without the DAPI counterstain to better visualize the p-Smad1/5 signal. **D** Immunofluorescence staining of the 15.5 dpc anterior small intestine from control and Foxl1 null mice for the WNT target gene *Sox9* (green), the proliferation marker Ki67 (red), and epithelial E-cadherin (white). Nuclei were counterstained with DAPI (blue). For imaging analyses (**C**, **D**), 3–5 embryos per genotype at the indicated developmental stages were examined, and representative images are shown.

this study were individually housed in ventilated cages and provided with controlled temperature, humidity, a 12 h light-dark cycle, a standard rodent chow diet, and constant access to water. C57BL/6 wild-type mice were obtained from Jackson Laboratory (Stock number: 000664). The Foxl1CreERT2-tdTomato gene replacement allele was described previously¹⁸.

For embryonic studies, embryonic day 0.5 (0.5 dpc) was defined as noon on the day when the copulatory plug was observed. Since homozygotes of the Foxl1CreERT2-tdTomato gene replacement allele are viable and fertile in adulthood, the Foxl1 null embryos were generated by either crossing two heterozygotes or crossing one homozygote with a heterozygote. Single cells for the Cut & Run experiment were isolated from dissected embryonic small intestines at 15.5 dpc, which were obtained by crossing Foxl1CreERT2-tdTomato heterozygous mice with C57BL/6 wild-type mice. Embryonic data were collected from developmental stages before (13.5 dpc), during (14.5 dpc), and after (15.5–18.5 dpc) the onset of villification in the developing small intestines. Due to the indistinguishable sex of the embryos and the absence of reported sex differences in villus morphogenesis, mice of both sexes were included in all experimental procedures. Therefore, random assignment of mice from either sex was conducted within each experimental group.

Tissue isolation and sectioning

Mouse small intestinal samples from different stages were carefully dissected. All samples used for histological sectioning and subsequent staining were taken from the anterior small intestine, from the stomach to the duodenal flexure, unless noted otherwise. For paraffin sections, samples were fixed overnight at 4 °C in 4% paraformaldehyde in PBS buffer (Invitrogen), washed three times with PBS before dehydration in a graded ethanol series and paraffin embedding. Tissues were sectioned at 5 μm thickness by the Molecular Pathology and Imaging Core of the UPenn Center for Molecular Studies in Digestive and Liver Diseases. For frozen sections, samples were incubated overnight in 30% sucrose in PBS buffer after overnight fixation at 4 °C in 4% paraformaldehyde in PBS buffer (Invitrogen) until the intestinal tissues had settled at the bottom of the tube, and were embedded in OCT for quick freezing and storage at –80 °C. OCT-embedded samples were sectioned at 10 μm using a cryostat (Cryostat NX50, ThermoFisher Scientific), dried for 10 minutes at room temperature, and then stored at –80 °C.

Scanning electron microscopy

The scanning electron microscope (SEM) experiments were conducted by the microscopy core facility of the UPenn Department of Cell and Developmental Biology. After dissection, the presumptive duodenal sections of 15.5 and 18.5 dpc fetuses and postnatal day 5 newborns were washed three times with 50 mM Na-cacodylate buffer and fixed overnight using a solution consisting of 2.5% glutaraldehyde in 50 mM Na-cacodylate buffer at a pH of 7.3. Subsequently, samples were dehydrated using a graded series of ethanol, gradually reaching 100%

ethanol over a span of 1.5 h. After dehydration, samples were incubated for 20 min in a solution containing 50% HMDS (Sigma-Aldrich) in ethanol, followed by three changes of 100% HMDS. After air-drying overnight, samples were mounted on stubs and coated with a layer of gold palladium using the sputter coating technique³⁵. Finally, we observed and photographed the specimens utilizing a Quanta 250 FEG scanning electron microscope manufactured by FEI (Hillsboro, OR, USA) with a 10 kV accelerating voltage.

Histology, immunofluorescence and TUNEL staining

Paraffin sections were deparaffinized and rehydrated using xylene and descending ethanol gradients. For H&E staining, tissues were stained with Harris' Hematoxylin and alcoholic Eosin Y. For IF staining, paraffin sections were subjected to pressure cooker antigen retrieval with Tris/EDTA buffer (Abcam, ab93684). For the frozen slices, OCT was directly removed in sterile water. The slices were then incubated with primary antibodies overnight at 4 °C after blocking with blocking buffer (Abcam, ab126587) for 1 h at room temperature and then with appropriate secondary antibodies at room temperature in the dark for 1 h.

The following antibodies were used: goat anti-PDGFR alpha 1: 200 (R&D Systems, AF1062), mouse anti-EZRIN 1:1000 (Sigma-Aldrich, E8897), rat anti-E-Cadherin antibody [DECMA-1] 1: 200 (Abcam, ab11512), goat anti-E-cadherin 1: 200 (R&D systems, AF-648), rabbit anti-Sox9 1: 200 (Abcam, ab185966), rabbit anti-Ki67 1: 200 (Abcam, ab16667), RFP antibody 1: 500 (Rockland, 600-401-379), Anterior gradient protein homolog 2 1: 200 (Abcam, ab209224), Muc2 1: 200 (Abcam, ab272692), Phospho-Smad1/5 1: 50 (Cell Signaling Technology, 9516), Alexa Fluor 488 Phalloidin 1: 400 (Thermo Fisher Scientific, A12379), Sal-like protein 1: 200 (Abcam, ab41974), Cleaved Caspase-3 1: 200 (Cell Signaling Technology), and Alexa Fluor 488-, 594- and 647-conjugated secondary antibodies, obtained from Life Technologies. Subsequently, slides were stained with DAPI (Sigma-Aldrich, D9542) to label nuclei. For F-actin staining, tissues were frozen-sectioned, treated with PBS followed by PBST (1:1000 Triton X-100 in PBS), followed by 1 h of staining with Alexa Fluor 488-conjugated Phalloidin diluted 1:1000 into the blocking buffer at room temperature. Slides were imaged using a Leica Stellaris 5 confocal microscope.

For the detection of Foxl1 protein, paraffin-embedded sections were deparaffinized in xylene and rehydrated through graded ethanol to PBS. Antigen retrieval was performed in Tris-EDTA buffer (pH 9.0) using a pressure cooker, followed by cooling and washing in PBS. Sections were permeabilized in PBST (PBS containing 0.1–0.2% Triton X-100) for 10–15 min and washed three times with PBS. Endogenous peroxidase was quenched with 3% H₂O₂ for 10–15 min, followed by PBS washes. Sections were blocked with blocking buffer (Abcam, ab126587) for 1 hour at room temperature.

Primary antibody against Foxl1 (guinea pig³⁶) was applied at 1:1500 dilution and incubated overnight at 4 °C. The antibody was detected using a biotinylated goat anti-guinea pig secondary antibody, followed by signal amplification using the biotin-avidin system (Vector Labs, SP-2001) and tyramide-based amplification (PerkinElmer,

Fig. 5 | Foxl1 is required for full activation of the planar cell polarity gene *Fat4* in small intestinal telocyte progenitors. **A** Small intestinal epithelial structure of the fetal small intestine in 15.5 dpc fetuses shows cuboidal organization of a single-cell layer epithelium. In *Foxl1* null mice, epithelial organization is disrupted, and the epithelium is partially multilayered, with frequent apoptotic cells, as visualized by cleaved caspase 3 immunostaining (green). The continued presence of telocytes is evidenced by Foxl1-tdTomato staining (red). DAPI (blue) was employed to visualize nuclei, and E-cadherin (white) to label epithelial cells. **B** Staining with the apical membrane marker Ezrin was used to identify T-folds, the sites of emerging villi, in the fetal (14.5 dpc) small intestine. **C** Quantification of T-fold number per linear distance of the small intestine. Data are presented as mean \pm standard deviation. $P = 0.0007$ by two-tailed unpaired t-test, $n = 4$ embryos per genotype. **D** Staining of the fetal (15.5 dpc) small intestine with F-actin was employed to determine the orientation of the dominant cellular axis in the mesenchyme of the developing

intestine. **E** UMAP and violin plots of expression of planar cell polarity genes *Fat4*, *Vangl1*, and *Vangl2* in control and Foxl1-deficient telocyte progenitors. Smooth muscle cells are shown for comparison. Statistical significance was assessed using a two-sided Wilcoxon rank-sum test. Smooth muscle cells (Control vs Foxl1 null): *Fat4*, ****, $p = 1.5 \times 10^{-13}$; *Vangl1*, ns, $p = 0.684$; *Vangl2*, ns, $p = 0.156$. Telocyte progenitor 1 (Control vs Foxl1 null): *Fat4*, ****, $p = 6.6 \times 10^{-7}$; *Vangl1*, ns, $p = 0.061$; *Vangl2*, ns, $p = 0.056$. Telocyte progenitor 2 (Control vs Foxl1 null): *Fat4*, ns, $p = 0.91$; *Vangl1*, ns, $p = 0.872$; *Vangl2*, ns, $p = 0.921$. *, $p < 0.05$; **, $p < 0.01$; ***, $p < 0.001$; ****, $p < 0.0001$. **F** Cut-and-Run analysis using anti-Foxl1 antibody and FACS enriched fetal (15.5 dpc) telocyte progenitors shows binding of Foxl1 at the *Fat4* promoter. For imaging analyses (**A**, **B**, and **D**), 3–5 embryos per genotype at the indicated developmental stages were examined, and representative images are shown. Cut&Run shown in (**F**) was performed using pooled telocyte progenitors isolated from E15.5 embryos.

number and viability were determined using a Countess II Automated Cell Counter from Life Technologies after staining with Trypan blue. Single-cell suspensions were diluted to the appropriate concentration and loaded on a 10x Genomics Chromium Single Cell Controller with a target of 5000 cells per sample. Single-cell library preparation was completed using the 10x Genomics Chromium Single Cell 3' Library & Gel Bead Kit v2 following the manufacturer's protocol. Quality and quantity of the cDNA libraries were assessed using an Agilent 2100 Bioanalyzer and Invitrogen Qubit Fluorometer. Finally, the libraries were sequenced on an Illumina Novaseq 6000 instrument. The single-cell RNA-seq data generated in this study have been deposited in GEO under accession number GSE302290.

Single-cell analysis workflow

Single-cell RNA sequencing (scRNAseq) libraries were prepared using the 10x Genomics Chromium platform and sequenced on a NovaSeq 6000 system with 150 bp paired-end reads. Each library was sequenced to a minimum depth of 361 million raw paired reads to ensure sufficient coverage for downstream analyses. Adapter trimming and read preprocessing were performed using Cutadapt³⁷, following the standard 10x Genomics configuration of 28 bp (cell barcode and unique molecular identifier [UMI]) and 90 bp (transcript read). For consistency, only the first 361 million raw paired reads for each sample were used for subsequent analyses. Trimmed reads were aligned to the mouse reference genome (mm10 release) using the Cell Ranger pipeline (v7.0.0)³⁸ with the `-include-introns false` parameter to exclude intronic reads. Gene-level expression matrices were generated for each sample.

To reduce technical noise and potential confounders, several stringent filtering steps were applied. Genes located on sex chromosomes (chrX and chrY) were excluded to minimize sex-specific expression effects. Ambient RNA contamination was estimated and removed using SoupX³⁹. Low-quality cells and potential doublets were filtered out by retaining only cells with total RNA counts (nCount_RNA) between 4,096 and 65,536. Cells with high mitochondrial gene expression (>10% of total RNA counts) were also excluded as indicators of cell stress or death.

Filtered expression matrices were integrated using the Seurat R package (v4.3.0)⁴⁰. Integration features were identified using SelectIntegrationFeatures and PrepSCTIntegration, and integration anchors were determined with FindIntegrationAnchors. The datasets were then merged using IntegrateData to correct for batch effects. Dimensionality reduction was conducted via principal component analysis (PCA). Clustering was performed using Uniform Manifold Approximation and Projection (UMAP) based on the top 20 principal components (as determined by elbow plots), followed by cluster identification with FindClusters (resolution = 0.5, method = 'igraph'). Cell type identities were assigned using scSorter⁴¹ with a manually curated list of canonical

marker genes. Assignments were refined by visual inspection of marker gene expression across clusters.

Cluster-specific differential gene expression analysis was performed using the FindMarkers function in Seurat with the Wilcoxon rank-sum test (test.use = "wilcox"). Expression levels of selected marker genes across telocyte progenitor cell clusters and smooth muscle cell clusters were visualized using violin plots. Statistical comparisons were performed using the stat_compare_means function from the rstatix R package⁴², applying Wilcoxon rank-sum tests for significance testing.

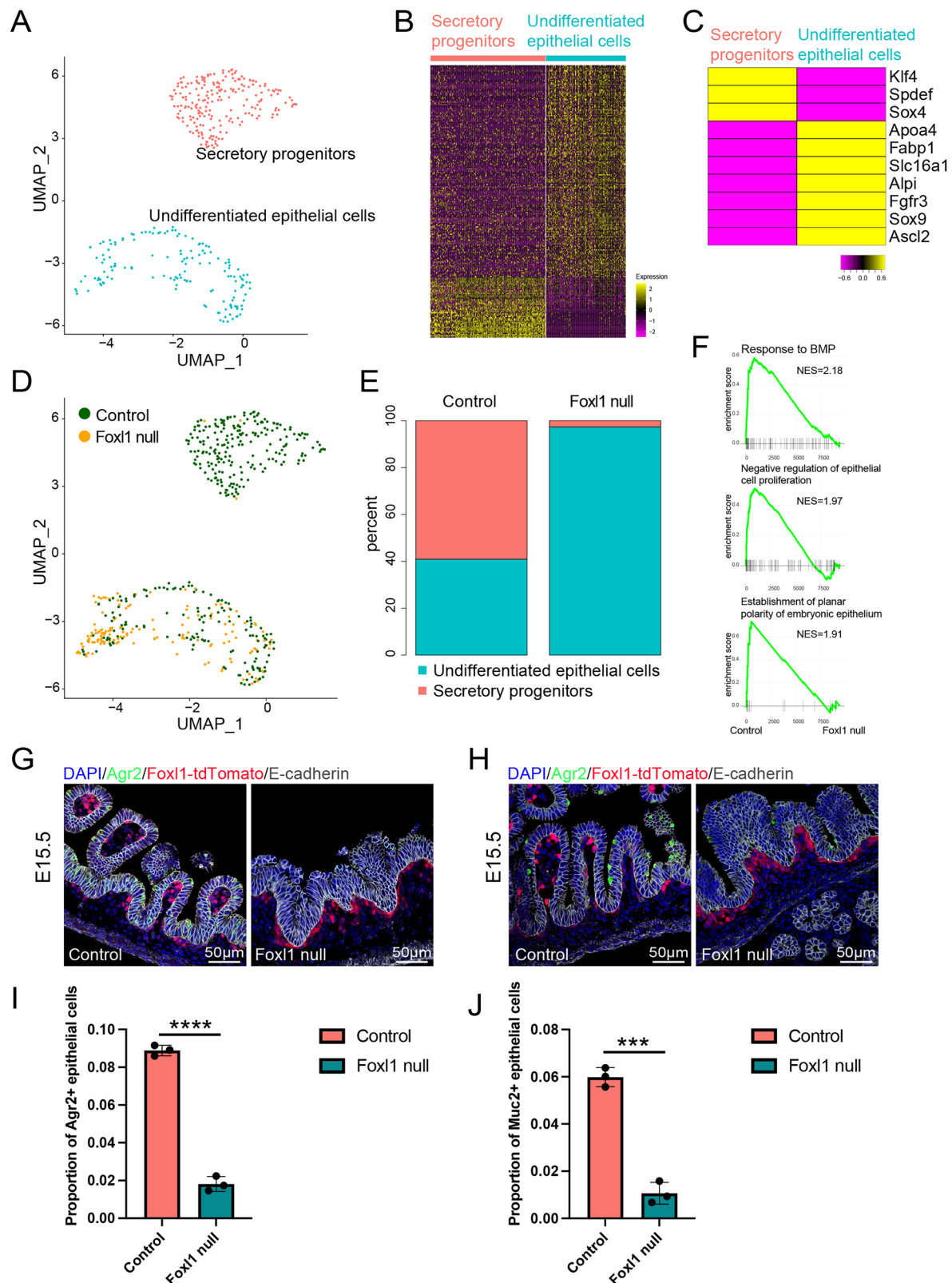
For RNA velocity analysis, spliced and unspliced reads were counted using Velocity (version 0.17.17)⁴³ based on the CellRanger output files. RNA velocity was then calculated with scVelo (version 0.3.3)²² using the stochastic model for gene-specific velocity estimation. Neighborhood graphs were computed using principal components derived from the integrated Seurat pipeline described above, and velocities were projected onto the same UMAP embedding to visualize predicted transitions between cell states. To better highlight the transcriptional dynamics within the telocyte progenitor compartment, velocity calculations were recomputed on selected clusters.

After QC filtering, the full dataset contained 8120 control and 7548 Foxl1-null cells. We also performed gene-expression analyses on selected combinations of mesenchymal clusters. The numbers of cells included in these clusters were as follows: Telocyte progenitor 1 (918 control, 502 mutant), Telocyte progenitor 2 (468 control, 478 mutant), Mesenchymal progenitor 1 (642 control, 827 mutant), Mesenchymal progenitor 2 (440 control, 302 mutant), and Smooth muscle (1293 control, 1375 mutant; combining Smooth muscle-1 and Smooth muscle-2). The specific cluster combinations analyzed are indicated in the corresponding figure panels. The analysis workflow used here is available via Zenodo (<https://zenodo.org/records/17713171>).

Cut & run and DNA product sequencing

Timed embryos were obtained by crossing *Foxl1* heterozygous male mice with C57BL/6 female mice. The entire length of the small intestine was digested with collagenase type II and DNase I dissolved in 'Dispase in DMEM/F-12' (Stemcell, 07923) to reach the single-cell state. Subsequently, the cells were sorted in phosphate-buffered saline with 0.5% BSA to enrich for tdTomato-positive cells using FACS (MoFlo Astrios Sorter).

Isolated tdTomato-positive telocytes from the embryonic small intestines at 15.5 dpc were subjected to CUT&RUN experiments. CUT&RUN experiments were performed using the CUT&RUN Assay Kit (EpiCypher, Catalog No. 14-1048) following the manufacturer's instructions using 40,000 telocyte progenitors. Anti-Foxl1, H3K4me3 positive control and rabbit IgG negative control antibodies (13-0042k) were used in these experiments. Purified CUT&RUN DNA products were subjected to the CUT&RUN Library Prep Kit (EpiCypher, 14-1002)



for library construction, and the libraries sequenced on an Illumina HiSeq X Ten instrument.

Single-molecule RNA fluorescent in situ hybridization

Proximal small intestinal sections from the *Foxl1* null mice and controls from the same litter were fixed and gradient dehydrated following the methods described above. To perform the single-

molecule RNA fluorescence in situ hybridization (smFISH), we employed the RNAScope Multiplex Fluorescent Reagent Kit v2 (323270) from Advanced Cell Diagnostics following the manufacturer's recommendations. smFISH imaging was performed using a confocal Leica Stellaris 5 microscope. The following RNAScope probes were obtained from Advanced Cell Diagnostics: *Foxl1* (C3) and *Glp2r* (C1).

Fig. 6 | Foxl1-dependent telocyte signals impact epithelial gene expression in the fetal gut. **A** UMAP plot of control epithelial cells from E15.5 embryos. The cells partition into two major clusters of secretory progenitors (red) and undifferentiated epithelial cells (blue). **B** Heatmap of the 255 genes differentially expressed between secretory progenitors and undifferentiated epithelial cells. Each row represents a gene, each column a cell. **C** Expression of key marker genes in secretory progenitors and undifferentiated epithelial cells. **D** UMAP plot of control (green) and *Foxl1* null (orange) epithelial cells. **E** Proportion of secretory progenitors and undifferentiated epithelial cells in control and *Foxl1* null embryos. **F** Gene set enrichment analysis (GSEA) identifies critical pathways normally active in fetal small intestinal epithelial cells as Foxl1 dependent. **G** Staining of the fetal (15.5 dpc)

small intestine with an antibody specific to Agr2 (Anterior gradient protein 2 homolog), a marker of the secretory lineage. **H** Staining of the fetal (15.5 dpc) small intestine with an antibody specific to Muc2 (Mucin 2), a marker of the goblet cell lineage. **I** Quantification of the proportion of Agr2-positive epithelial cells of all epithelial cells (DAPI/E-cadherin double positive) in the 15.5.dpc anterior small intestine. $N = 3$ embryos per genotype, $p < 0.0001$ by two-tailed unpaired t-test with Welch's correction. **J** Quantification of the proportion of Muc2-positive epithelial cells of all epithelial cells (DAPI/E-cadherin double positive) in the 15.5. dpc anterior small intestine. $N = 3$ embryos per genotype. Data are presented as mean \pm standard deviation. $p = 0.0002$ by two-tailed unpaired t-test with Welch's correction.

Whole-mount immunostaining

Fetal small intestine segments were fixed in 4% PFA at 4 °C overnight, then rehydrated in PBS. Tissues were permeabilized and blocked in 1× blocking buffer (ab126587) for 24 h at 4 °C. Tissues were incubated with the primary antibody (anti-Pdgfra, R&D Systems, AF1062) in the same buffer for 48 h, followed by overnight washes in PBS containing 0.5% Triton X-100. Secondary antibodies were applied for 48 h, followed by overnight washes with 0.5% Triton X-100. Nuclei were counterstained with DAPI where indicated. Tissues were then dehydrated in methanol and cleared in a 1:2 mixture of benzyl alcohol and benzyl benzoate (BABB) through a series of brief exchanges. Cleared samples were mounted in Fast Wells (FW20 or 25 × 25 mm, Grace Biolabs) and imaged by z-stack confocal microscopy (Leica Stellaris 5).

Statistical analysis

For comparisons between two groups (WT vs. *Foxl1* null), we used a two-tailed unpaired t-test with Welch's correction using GraphPad Prism 10. Data are presented as mean \pm SEM unless otherwise indicated. Expression levels of selected marker genes across specific cell clusters were visualized using violin plots. Statistical comparisons were performed using the `stat_compare_means` function from the `rstatix` R package⁴², applying Wilcoxon rank-sum tests for significance testing.

Data availability

The single-cell RNA sequencing datasets generated in this study are available in the NCBI Gene Expression Omnibus (GEO) under accession number GSE302290. A source data file is provided. All other relevant data supporting the findings of this study are available from the corresponding author upon request. Source data are provided with this paper.

References

- Helander, H. F. & Fandriks, L. Surface area of the digestive tract—revisited. *Scand. J. Gastroenterol.* **49**, 681–689 (2014).
- Shyer, A. E., Huycke, T. R., Lee, C., Mahadevan, L. & Tabin, C. J. Bending gradients: how the intestinal stem cell gets its home. *Cell* **161**, 569–580 (2015).
- Shyer, A. E. et al. Villification: how the gut gets its villi. *Science* **342**, 212–218 (2013).
- Walton, K. D., Mishkind, D., Riddle, M. R., Tabin, C. J. & Gumucio, D. L. Blueprint for an intestinal villus: Species-specific assembly required. *Wiley Interdiscip. Rev. Dev. Biol.* **7**, e317 (2018).
- Karlsson, L., Lindahl, P., Heath, J. K. & Betsholtz, C. Abnormal gastrointestinal development in PDGF-A and PDGFR- α deficient mice implicates a novel mesenchymal structure with putative instructive properties in villus morphogenesis. *Development* **127**, 3457–3466 (2000).
- Walton, K. D., Freddo, A. M., Wang, S. & Gumucio, D. L. Generation of intestinal surface: an absorbing tale. *Development* **143**, 2261–2272 (2016).
- Walton, K. D. et al. Hedgehog-responsive mesenchymal clusters direct patterning and emergence of intestinal villi. *Proc. Natl. Acad. Sci. USA* **109**, 15817–15822 (2012).
- Freddo, A. M. et al. Coordination of signaling and tissue mechanics during morphogenesis of murine intestinal villi: a role for mitotic cell rounding. *Integr. Biol.* **8**, 918–928 (2016).
- Grosse, A. S. et al. Cell dynamics in fetal intestinal epithelium: implications for intestinal growth and morphogenesis. *Development* **138**, 4423–4432 (2011).
- Walton, K. D. et al. Villification in the mouse: Bmp signals control intestinal villus patterning. *Development* **143**, 427–436 (2016).
- Huycke, T. R. et al. Patterning and folding of intestinal villi by active mesenchymal dewetting. *Cell* **187**, 3072–3089 e3020 (2024).
- Mathan, M., Moxey, P. C. & Trier, J. S. Morphogenesis of fetal rat duodenal villi. *Am. J. Anat.* **146**, 73–92 (1976).
- Guiu, J. et al. Tracing the origin of adult intestinal stem cells. *Nature* **570**, 107–111 (2019).
- Madison, B. B. et al. Epithelial hedgehog signals pattern the intestinal crypt-villus axis. *Development* **132**, 279–289 (2005).
- Kaestner, K. H., Silberg, D. G., Traber, P. G. & Schutz, G. The mesenchymal winged helix transcription factor Fkh6 is required for the control of gastrointestinal proliferation and differentiation. *Genes Dev.* **11**, 1583–1595 (1997).
- Kondo, A. & Kaestner, K. H. FoxL1(+) mesenchymal cells are a critical source of Wnt5a for midgut elongation during mouse embryonic intestinal development. *Cells Dev.* **165**, 203662 (2021).
- Madison, B. B., McKenna, L. B., Dolson, D., Epstein, D. J. & Kaestner, K. H. FoxF1 and FoxL1 link hedgehog signaling and the control of epithelial proliferation in the developing stomach and intestine. *J. Biol. Chem.* **284**, 5936–5944 (2009).
- Kolev, H. M. et al. A FoxL1-CreERT-2A-tdTomato Mouse Labels Subepithelial Telocytes. *Cell Mol. Gastroenterol. Hepatol.* **12**, 1155–1158 e1154 (2021).
- Katz, J. P. et al. Foxl1 null mice have abnormal intestinal epithelia, postnatal growth retardation, and defective intestinal glucose uptake. *Am. J. Physiol. Gastrointest. Liver Physiol.* **287**, G856–G864 (2004).
- Perreault, N., Katz, J. P., Sackett, S. D. & Kaestner, K. H. Foxl1 controls the Wnt/ β -catenin pathway by modulating the expression of proteoglycans in the gut. *J. Biol. Chem.* **276**, 43328–43333 (2001).
- Perreault, N., Sackett, S. D., Katz, J. P., Furth, E. E. & Kaestner, K. H. Foxl1 is a mesenchymal Modifier of Min in carcinogenesis of stomach and colon. *Genes Dev.* **19**, 311–315 (2005).
- Bergen, V., Lange, M., Peidli, S., Wolf, F. A. & Theis, F. J. Generalizing RNA velocity to transient cell states through dynamical modeling. *Nat. Biotechnol.* **38**, 1408–1414 (2020).
- He, X. C. et al. BMP signaling inhibits intestinal stem cell self-renewal through suppression of Wnt- β -catenin signaling. *Nat. Genet.* **36**, 1117–1121 (2004).
- Wang, S., Cebrian, C., Schnell, S. & Gumucio, D. L. Radial WNT5A-Guided Post-mitotic Filopodial Pathfinding Is Critical for Midgut Tube Elongation. *Dev. Cell* **46**, 173–188 e173 (2018).
- Rao-Bhatia, A. et al. Hedgehog-activated Fat4 and PCP pathways mediate mesenchymal cell clustering and villus formation in gut development. *Dev. Cell* **52**, 647–658 e646 (2020).

26. Gracz, A. D. et al. Sox4 promotes Atoh1-independent intestinal secretory differentiation toward tuft and enteroendocrine fates. *Gastroenterology* **155**, 1508–1523 e1510 (2018).
27. Gregorieff, A. et al. The ets-domain transcription factor Spdef promotes maturation of goblet and paneth cells in the intestinal epithelium. *Gastroenterology* **137**, 1333–1345 e1331–1333 (2009).
28. Katz, J. P. et al. The zinc-finger transcription factor Klf4 is required for terminal differentiation of goblet cells in the colon. *Development* **129**, 2619–2628 (2002).
29. Motoyama, J. et al. Overlapping and non-overlapping Ptch2 expression with Shh during mouse embryogenesis. *Mech. Dev.* **78**, 81–84 (1998).
30. Ramalho-Santos, M., Melton, D. A. & McMahon, A. P. Hedgehog signals regulate multiple aspects of gastrointestinal development. *Development* **127**, 2763–2772 (2000).
31. Hallikas, O. et al. Genome-wide prediction of mammalian enhancers based on analysis of transcription-factor binding affinity. *Cell* **124**, 47–59 (2006).
32. Maimets, M. et al. Mesenchymal-epithelial crosstalk shapes intestinal regionalisation via Wnt and Shh signalling. *Nat. Commun.* **13**, 715 (2022).
33. Shoshkes-Carmel, M. et al. Subepithelial telocytes are an important source of Wnts that supports intestinal crypts. *Nature* **557**, 242–246 (2018).
34. Ormestad, M. et al. Foxf1 and Foxf2 control murine gut development by limiting mesenchymal Wnt signaling and promoting extracellular matrix production. *Development* **133**, 833–843 (2006).
35. Braet, F., De Zanger, R. & Wisse, E. Drying cells for SEM, AFM and TEM by hexamethyldisilazane: a study on hepatic endothelial cells. *J. Microsc.* **186**, 84–87 (1997).
36. Aoki, R. et al. Foxl1-expressing mesenchymal cells constitute the intestinal stem cell niche. *Cell Mol. Gastroenterol. Hepatol.* **2**, 175–188 (2016).
37. Martin M. Cutadapt removes adapter sequences from high-throughput sequencing reads. *2011* **17**, 3 (2011).
38. Zheng, G. X. et al. Massively parallel digital transcriptional profiling of single cells. *Nat. Commun.* **8**, 14049 (2017).
39. Young M. D., Behjati S. SoupX removes ambient RNA contamination from droplet-based single-cell RNA sequencing data. *Gigascience* **9**, (2020).
40. Hao, Y. et al. Integrated analysis of multimodal single-cell data. *Cell* **184**, 3573–3587 e3529 (2021).
41. Guo, H. & Li, J. scSorter: assigning cells to known cell types according to marker genes. *Genome Biol.* **22**, 69 (2021).
42. Kassambara, A. rstatix: Pipe-Friendly. *Framework for Basic Statistical Tests*, (2023).
43. La Manno, G. et al. RNA velocity of single cells. *Nature* **560**, 494–498 (2018).

Acknowledgements

We thank members of the Kaestner lab for helpful discussions. This work was supported by NIH grants R37DK053839 and R01DK139049. We

thank the UPenn Center for Molecular Studies in Digestive and Liver Diseases (P30 DK050306) for the use of the Molecular Pathology and Imaging Core (MPIC) for tissue processing, the UPenn Diabetes Research Center Functional Genomics Core (P30 DK019125) for help with data analysis, and Yuri Veklich from the Cell & Developmental Biology Microscopy Core in the UPenn Department of Cell Biology for the use of their scanning electron microscope and confocal imaging services.

Author contributions

G.Z. and K.H.K.—Conceptualization and writing. G.Z., G.R., K.B., M.T., L.C. and D.L.—Methodology. G.Z. and J.S.—Data curation and visualization. K.H.K.—Supervision. K.H.K.—Funding acquisition.

Competing interests

The authors declare no competing interests.

Additional information

Supplementary information The online version contains supplementary material available at <https://doi.org/10.1038/s41467-026-69791-5>.

Correspondence and requests for materials should be addressed to Klaus H. Kaestner.

Peer review information *Nature Communications* thanks the anonymous reviewers for their contribution to the peer review of this work. A peer review file is available.

Reprints and permissions information is available at <http://www.nature.com/reprints>

Publisher's note Springer Nature remains neutral with regard to jurisdictional claims in published maps and institutional affiliations.

Open Access This article is licensed under a Creative Commons Attribution-NonCommercial-NoDerivatives 4.0 International License, which permits any non-commercial use, sharing, distribution and reproduction in any medium or format, as long as you give appropriate credit to the original author(s) and the source, provide a link to the Creative Commons licence, and indicate if you modified the licensed material. You do not have permission under this licence to share adapted material derived from this article or parts of it. The images or other third party material in this article are included in the article's Creative Commons licence, unless indicated otherwise in a credit line to the material. If material is not included in the article's Creative Commons licence and your intended use is not permitted by statutory regulation or exceeds the permitted use, you will need to obtain permission directly from the copyright holder. To view a copy of this licence, visit <http://creativecommons.org/licenses/by-nc-nd/4.0/>.

© The Author(s) 2026